PAPER

Check for updates

Rechargeable asymmetric zinc–nitrate/glycerol batteries synergizing chemical valorization and energy conversion

Zhijie Yan,[a] Shuoyi Chen,[a] Weijie Mei,[a] Yaqiong Wu,[a] Yaning Qie,[a] Huilin Ge,[a] Fangbing Li,[a] Zengyu Luo,[a] Feifei Wang*[b] and Chunpeng Yang [ID] *[a]

Aqueous rechargeable zinc (Zn)-based batteries are promising for safe and sustainable energy storage. In addition to energy storage, Zn-based batteries, such as Zn–nitrate batteries and Zn–CO$_2$ batteries, can be utilized for value-adding electro-reduction reactions, but their rechargeability and cycling stability are limited by inefficient and irreversible charging reactions, particularly the sluggish oxygen evolution reaction (OER). Here, we propose rechargeable asymmetric Zn batteries (aZBs) as a novel strategy for simultaneously achieving energy storage and chemical valorization. As a proof of concept, our aZB employs an asymmetric redox configuration to replace the energy-intensive OER with a thermodynamically favorable and value-generating glycerol oxidation reaction (GOR). This dual-function asymmetric battery configuration enables low-voltage charging and high energy efficiency while producing ammonia and formic acid during discharge and charge, respectively—two chemicals with widespread applications in agriculture, pharmaceuticals, and clean fuel systems. Assisted by a bifunctional electrocatalyst, the system delivers an energy efficiency of 62.2% and a stable cycling lifespan of over 200 hours at 2 mA cm^{-2}. Flow-cell aZBs demonstrate continuous discharging/value-adding cycles for 120 h at 5 mA cm^{-2}, showcasing the potential for the sustainable coproduction of value-added chemicals. This work establishes a new battery design paradigm that synergizes asymmetric redox reactions and biomass-derived molecule utilization, paving the way for integrated energy–chemical co-production systems beyond traditional reversible redox battery configurations.

Broader context

Aqueous Zn-based batteries are considered promising candidates for clean and sustainable energy storage because of their safety, low cost, and use of earth-abundant materials. Beyond electricity storage, integrating these systems with chemical production offers an opportunity to improve energy efficiency and generate value-added products. Here, we demonstrate a rechargeable asymmetric Zn battery that couples the nitrate reduction reaction with the glycerol oxidation reaction. This design not only lowers the charging energy input and enhances cycling efficiency, but also enables the simultaneous production of ammonia and formic acid, two chemicals of broad industrial relevance. By bridging energy storage with chemical valorization, this work introduces a new paradigm for Zn-based batteries as integrated platforms for sustainable energy–chemical co-production.

Introduction

Aqueous zinc (Zn)-based rechargeable batteries (AZBs) have garnered increasing attention as next-generation energy storage devices, owing to their intrinsic safety, low cost, environmental friendliness, and use of Earth-abundant

[a]Tianjin Key Laboratory of Advanced Carbon and Electrochemical Energy Storage, School of Chemical Engineering and Technology, and National Industry-Education Integration Platform of Energy Storage, Tianjin University, Tianjin 300350, China. E-mail: cpyang@tju.edu.cn
[b]Max Planck Institute for Microstructure Physics, Halle (Saale) D-06120, Germany. E-mail: Feifei.Wang@mpi-halle.mpg.de

materials.[1–6] In addition to the function of energy storage, new avenues for integrating electrochemical energy storage with chemical valorization and environmental remediation have been demonstrated by Zn–nitrate batteries (ZNBs) and Zn–CO$_2$ batteries.[7] Taking ZNBs as a typical example, during discharge, the nitrate reduction reaction (NO$_3$RR) converts nitrate pollutants into value-added ammonia (NH$_3$), offering both electricity generation and pollutant revalorization.[8–12] This dual benefit positions ZNBs as a promising solution for sustainable energy–environmental coupling. Despite their potential, ZNBs face critical limitations in the charging process, during which the cell must drive an oxidation reaction to accept electrons and nearly all current designs choose the oxygen-evolution

reaction (OER) for this task.[13–16] However, the OER is intrinsically sluggish, demands large overpotentials, and produces only low-value oxygen gas.[17,18] Moreover, the thermodynamic and kinetic challenges of ammonia oxidation render it irreversible under practical conditions, ultimately undermining the NO_3^--to-NH_3 conversion objective.[19]

In recent years, small-molecule oxidation reactions (SMORs) have emerged as attractive alternatives to the OER due to their lower oxidation potentials and ability to generate valuable chemicals.[20–25] For example, the glycerol oxidation reaction (GOR) has received extensive attention due to its low oxidation potential (−0.69 V *vs.* SHE) and ability to generate value-added chemicals such as formic acid and glycolic acid.[26–29] By pairing SMORs with cathodic reductions like hydrogen evolution or CO_2 reduction, electrolyzer systems have demonstrated improved energy efficiency and enhanced economic returns.[30–32] However, these efforts have been largely restricted to primary electrochemical cells (*e.g.*, water electrolysis) rather than rechargeable secondary battery systems.[33,34] The integration of SMORs such as the GOR into rechargeable batteries, especially Zn-based architectures involving NO_3^- reduction, remains virtually unexplored. This is primarily due to fundamental challenges in redox potential matching, charge balancing, interfacial stability, and maintaining reversibility over extended cycling. Therefore, a significant gap persists in the development of full-cell battery systems that can simultaneously co-produce value-added chemicals and store renewable energy using coupled SMOR/NO_3RR strategies.

Here, we bridge that gap with a rechargeable asymmetric Zn–nitrate/glycerol battery (aZB) that integrates the electrochemical NO_3RR and GOR to enable full-process chemical valorization and energy conversion (Fig. 1). In this system, the half-reaction reduces NO_3^- to NH_3 during discharge, while the half-reaction oxidizes glycerol into high-value formic acid (HCOOH) during charging. This asymmetric redox configuration replaces the conventional OER with a thermodynamically favorable and productive pathway, lowering the charging voltage and enhancing energy efficiency. Notably, the battery achieves co-generation of two value-added products in a single device: NH_3 as a fertilizer or refrigerant, and HCOOH as a platform chemical or fuel for direct formic acid fuel cells. Since both the NO_3RR and the GOR must proceed with fast kinetics and low overpotentials in the same electrolyte, a bifunctional catalyst is required to couple the two reactions efficiently. For this purpose, we constructed a CuO_x/NiCo layered double hydroxide (CuO_x/NiCoLDH) composite, leveraging the individual prowess of its constituent elements (Cu, Ni, and Co), all recognized for their high activity in both the NO_3RR and the GOR. With this catalyst, the aZB attains 62.2% energy efficiency, robust rate capability, and stable operation for over 200 h at 2 mA cm^{-2}. When implemented in a flow-cell architecture, the aZB operated stably for 120 h at a current density of
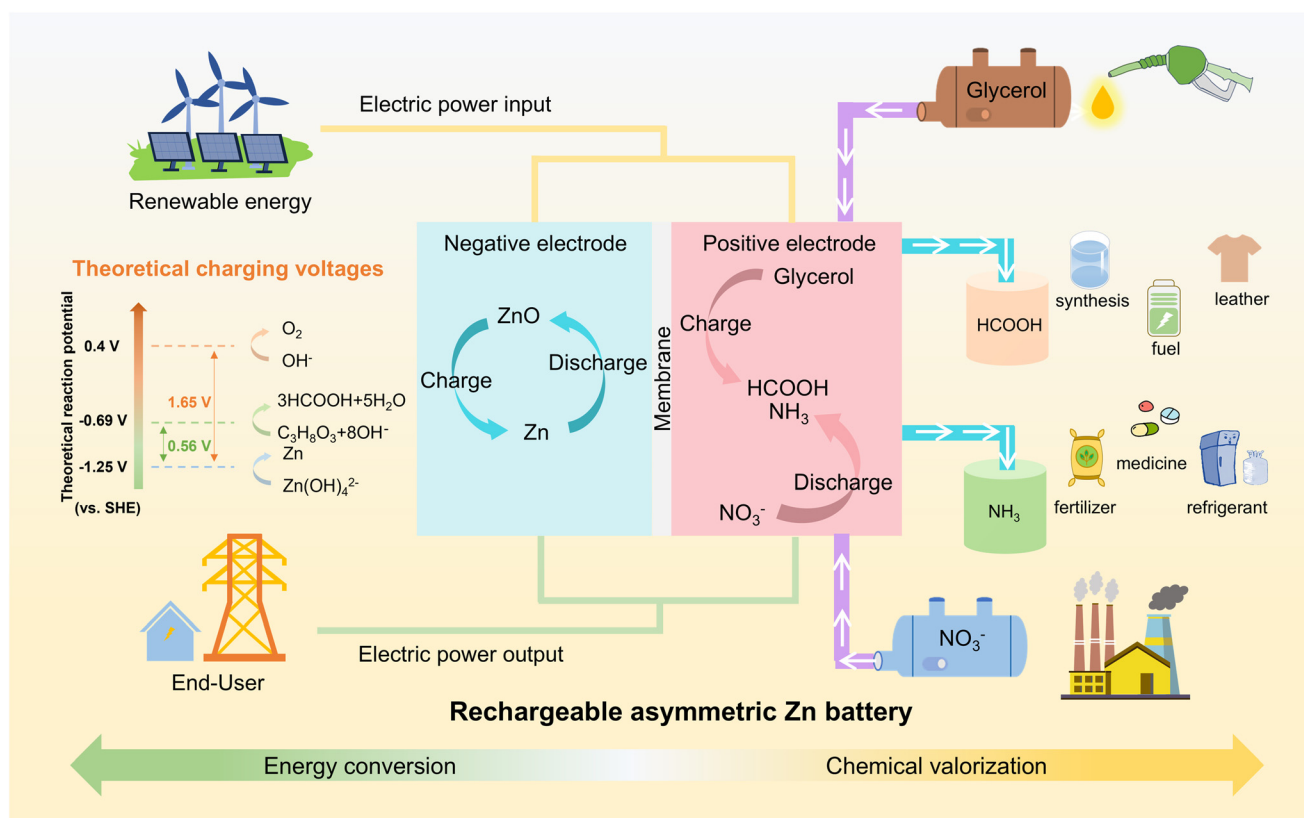

Fig. 1 Schematic illustration of an asymmetric Zn battery for green energy conversion and high-value-added chemical production.

5 mA cm^{-2}, showcasing the scalability of the concept. This work pioneers a new battery design paradigm that strategically couples asymmetric redox reactions for simultaneous energy storage and chemical production.

Results and discussion

Synthesis and characterization of electrocatalysts

To demonstrate the feasibility of asymmetric redox coupling in aqueous Zn batteries, we constructed a proof-of-concept rechargeable aZB using a Zn foil negative electrode, a Nafion 117 membrane as the separator, and a catalyst positive electrode (Fig. 2a). During discharge, NO_3^- is electrochemically reduced to NH_3, while during charging, glycerol (Gly) is oxidized to HCOOH, according to the following half-reactions:

$$NO_3^- + 6H_2O + 8e^- \rightarrow NH_3 + 9OH^- \quad (1)$$

$$C_3H_8O_3 + 8OH^- \rightarrow 3HCOOH + 5H_2O + 8e^- \quad (2)$$

Given the dual redox functions, the electrocatalyst plays a pivotal role in enabling efficient NO_3^- reduction and glycerol oxidation. We designed and synthesized a bifunctional CuO_x/NiCoLDH catalyst by a wet-chemical precipitation strategy. X-ray diffraction (XRD) analysis confirms the coexistence of crystalline Cu-based phases and the amorphous LDH domain (Fig. 2b). Diffraction peaks at 43.3° and 50.4° are indexed to the (111) and (200) planes of Cu (PDF#04-0836), while those at 36.4°, 61.3° and 73.5° correspond to the (111), (220) and (311) planes of Cu_2O (PDF#05-0667).[35,36] The weak diffraction peaks at 33.4° and 60° are assigned to the (101) and (110) planes of NiCoLDH (PDF#38-0715), indicating a partial crystalline LDH domain.[37] Inductively coupled plasma optical emission spectrometry (ICP-OES) indicates that the Ni : Co : Cu weight ratio is 1 : 1 : 1. When CuO_x or NiCoLDH is synthesised individually, its XRD pattern contains only the respective individual charac-
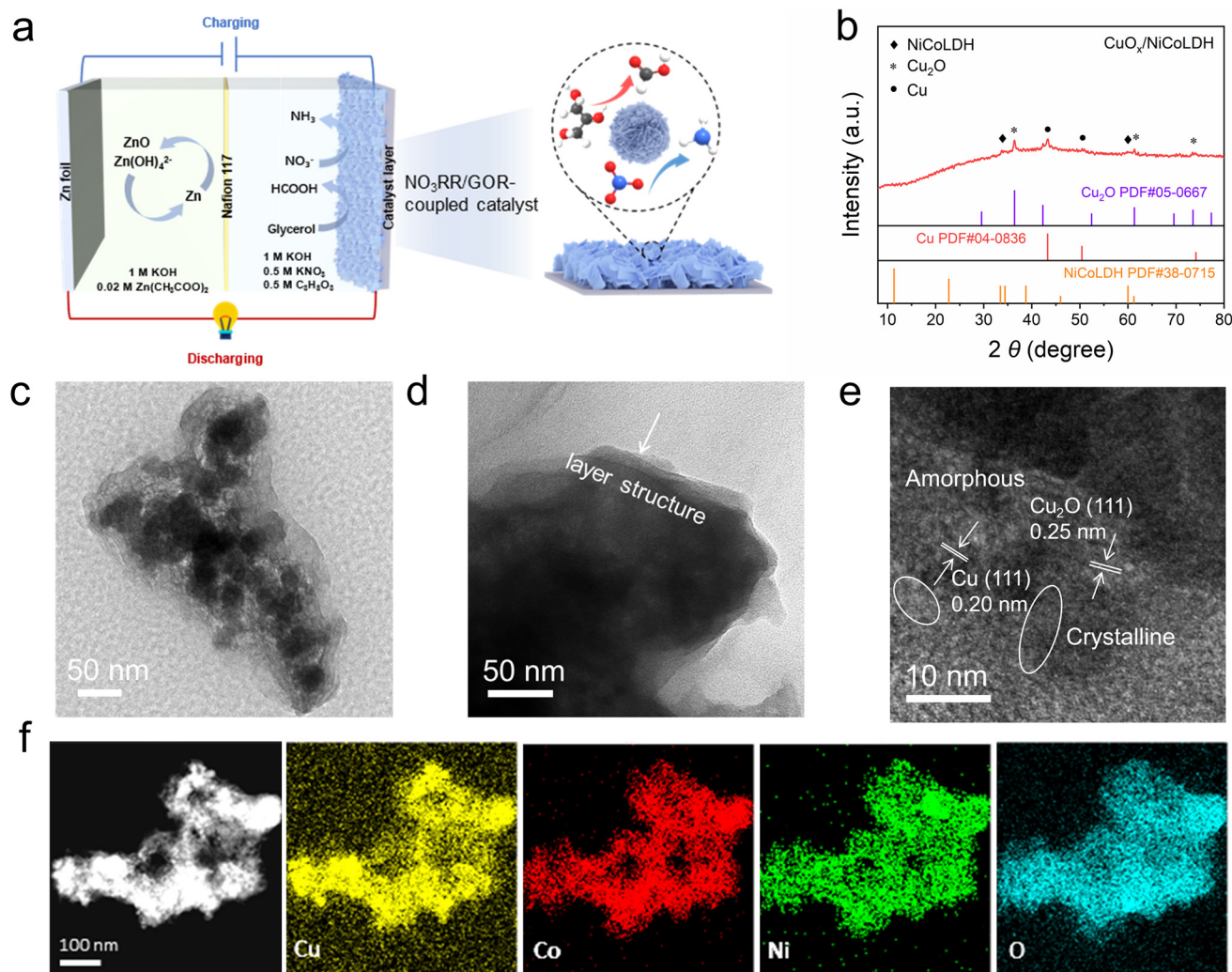

Fig. 2 Structural and morphological characterization of the aZB configuration and CuO_x/NiCoLDH catalyst. (a) Scheme illustration of the rechargeable aZB configuration. (b) XRD pattern of the CuO_x/NiCoLDH composite. (c) and (d) TEM image of CuO_x/NiCoLDH. (e) HRTEM and (f) EDS mapping of the bifunctional CuO_x/NiCoLDH electrocatalyst.

teristic reflections (Fig. S1). The simultaneous presence of both Cu-based and LDH peaks in the composite therefore confirms that the two phases are chemically integrated, rather than being a physical mixture of discrete phases.

Scanning electron microscopy (SEM) images reveal that the CuO_x/NiCoLDH catalyst shows a well-defined three-dimensional flower-like microsphere structure, composed of ultrathin nanosheets (Fig. S2), which is also confirmed by transmission electron microscopy (TEM) (Fig. 2c and d). This three-dimensional hierarchically porous structure with a smaller size provides a larger specific surface area, exposing more active sites. High-resolution TEM (HRTEM) reveals distinct lattice fringes with spacings of 0.25 nm and 0.20 nm, corresponding to the (111) planes of Cu_2O and metallic Cu, respectively, embedded within an amorphous LDH matrix (Fig. 2e). The fast Fourier transform (FFT) pattern of the same area again

matches those of Cu and Cu_2O (Fig. S3). Elemental mapping reveals a uniform distribution of Cu, Ni, Co and O throughout the microsphere (Fig. 2f), indicating that CuO_x nanocrystals and NiCoLDH are intergrown rather than segregated. These results confirm that the wet-chemical route yields a hybrid comprising crystalline CuO_x domains dispersed within an amorphous NiCoLDH framework.

Electrochemical performance measurements

To investigate the bifunctional NO_3RR/GOR performance for the NO_3RR and GOR, a series of electrochemical measurements was performed in an H-type cell. Linear sweep voltammetry (LSV) curves reveal that all catalysts exhibit higher response currents and lower overpotentials with the addition of NO_3^-, indicating efficient NO_3RR activity (Fig. 3a). Notably, CuO_x/NiCoLDH required only 0.168 V (vs. RHE) to reach 10 mA
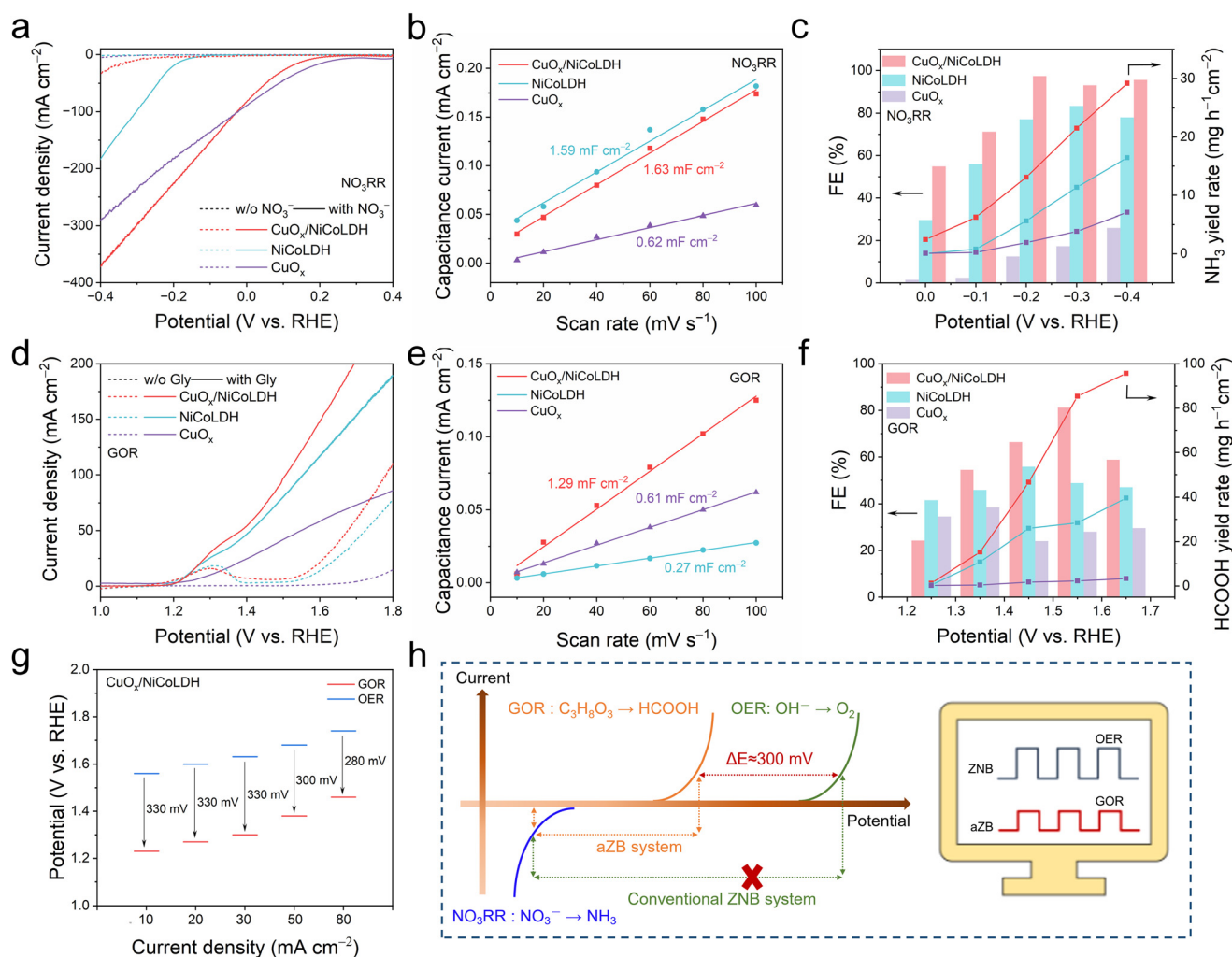

Fig. 3 Electrochemical performance for the NO_3RR and GOR with CuO_x/NiCoLDH, NiCoLDH, and CuO_x catalysts. (a) NO_3RR LSV curves in 1.0 M KOH with (solid lines) and without (dashed lines) 0.5 M KNO_3. (b) Fitting results of double-layer capacitance (C_{dl}). (c) FE (NH_3) and NH_3 yield rate at different applied potentials. (d) GOR LSV curves in 1.0 M KOH with (solid lines) and without (dashed lines) 0.5 M glycerol. (e) Fitting results of double-layer capacitance (C_{dl}). (f) FE (HCOOH) and HCOOH yield rate at different applied potentials. (g) Comparisons of the oxidation potentials to achieve varied current densities in 1 M KOH with (GOR) and without (OER) 0.5 M glycerol addition. (h) Schematic illustration of polarization curves for the NO_3RR, GOR, and OER, and corresponding comparison of the charge–discharge profiles of conventional ZNBs and aZBs.

cm^{-2}, significantly less negative than that required for NiCoLDH (−0.175 V $vs.$ RHE) yet slightly higher than that of CuO$_x$ (0.24 V $vs.$ RHE). The electrochemically active surface areas (ECSAs), estimated from electrochemical double-layer capacitance (C_{dl}), show that CuO$_x$/NiCoLDH (1.63 mF cm^{-2}) possesses more accessible active sites than NiCoLDH (1.59 mF cm^{-2}) and CuO$_x$ (0.62 mF cm^{-2}) (Fig. 3b and Fig. S4). Tafel plots derived from the LSV curves show a slope of 143 mV dec^{-1} for CuO$_x$/NiCoLDH, which is intermediate between NiCoLDH (96 mV dec^{-1}) and CuO$_x$ (200 mV dec^{-1}) (Fig. S5). The high Tafel slope of pure CuO$_x$ identifies the initial NO$_3^-$-to-NO$_2^-$ step as its rate-determining step, while the low slope of NiCoLDH reflects rapid proton–electron delivery, consistent with its superior water-dissociation kinetics. Accordingly, we propose that the moderate slope of CuO$_x$/NiCoLDH is not a mere statistical compromise, but rather the kinetic signature of a bifunctional synergy: CuO$_x$ facilitates the formation of the NO$_2^-$ intermediate,[38–40] while NiCoLDH indicates its superior electron transfer efficiency, which is beneficial for the subsequent reduction of NO$_2^-$ to NH$_3$.[41–44] The rapid consumption of the NO$_2^-$ intermediate by NiCoLDH drives the upstream nitrate reduction, thereby alleviating the kinetic limitation of the rate-determining step on CuO$_x$ and leading to an overall acceleration of the reaction kinetics, as corroborated by the NO$_3$RR performance. The NO$_3$RR performance was further evaluated by chronoamperometry measurement for 1 h in the potential range from 0 to −0.4 V ($vs.$ RHE). Ammonia produced during each run was quantified by UV-vis spectroscopy using the calibration curve (Fig. S6 and S7). The CuO$_x$/NiCoLDH delivers the highest FE (NH$_3$) of 97.3% at −0.2 V ($vs.$ RHE). Correspondingly, the NH$_3$ yield rate peaked at 30 mg h^{-1} cm^{-2} at −0.4 V ($vs.$ RHE), nearly 1.87 and 4.28 times higher than those of NiCoLDH and CuO$_x$, respectively, confirming the superior NO$_3$RR performance of CuO$_x$/NiCoLDH due to the synergistic effect of NiCoLDH and CuO$_x$ and indirectly verifying our hypothesis about the Tafel slope (Fig. 3c). Specifically, the active phase of CuO$_x$ is responsible for the NO$_3^-$ adsorption, activation and reduction, while NiCoLDH is responsible for the water dissociation to provide abundant active *H for the hydrogenation step in the NO$_3$RR process, thereby boosting the NO$_3$RR performance.

We further evaluate the GOR performance of CuO$_x$/NiCoLDH in a three-electrode system using a 1 M KOH/0.5 M glycerol electrolyte. LSV curves reveal that CuO$_x$/NiCoLDH exhibits superior activity with a low potential of 1.23 V ($vs.$ RHE) at 10 mA cm^{-2}, outperforming NiCoLDH (1.24 V $vs.$ RHE) and CuO$_x$ (1.30 V $vs.$ RHE) (Fig. 3d). Additionally, CuO$_x$/NiCoLDH exhibits the lowest Tafel slope of 77 mV dec^{-1} among the three catalysts, validating faster reaction kinetics (Fig. S8). The C_{dl} is 1.29 mF cm^{-2} for CuO$_x$/NiCoLDH, substantially higher than that of either single-phase reference (Fig. 3e and Fig. S9), indicating a larger number of accessible catalytic sites. To determine the value-added oxidation products, chronoamperometric tests were conducted at varied potentials, followed by ^{1}H nuclear magnetic resonance (NMR) analysis (Fig. S10). The FE (HCOOH) production reaches 81.2% at 1.55 V with CuO$_x$/

NiCoLDH, outperforming NiCoLDH (48.8%) and CuO$_x$ (28.0%), highlighting its excellent product selectivity (Fig. 3f). The performance enhancement, arising from the synergy between NiCoLDH and CuO$_x$, is achieved both by an increase in the ECSA, which provides more reactive sites, and by steering of the reaction pathway toward formic acid production, which improves selectivity. More specifically, the onset potential of the GOR is significantly reduced compared to the OER, particularly with CuO$_x$/NiCoLDH, confirming its advantage in lowering charge voltages for asymmetric batteries (Fig. 3g). Due to the much lower operative potential for the GOR than that of the OER and the exceptional performance of CuO$_x$/NiCoLDH, the unique configuration coupled with the NO$_3$RR and GOR is expected to effectively decrease charging voltage and upgrade low-value chemicals (Fig. 3h). Thus, the CuO$_x$/NiCoLDH catalyst exhibits high activity for the NO$_3$RR and GOR through a synergistic mechanism, outperforming all individual components. LSV was also used to investigate the catalytic performance of CuO$_x$/NiCoLDH in electrolytes where nitrate and glycerol coexisted, which demonstrates that CuO$_x$/NiCoLDH can maintain superior bifunctional performance under mixed-substrate conditions, validating its applicability for aZBs (Fig. S11).

Rechargeable asymmetric zinc–nitrate/glycerol battery performance

Taking advantage of the bifunctional activity of CuO$_x$/NiCoLDH, we assembled a rechargeable aZB in an H-type cell (Fig. 4a). In this configuration, the composite catalyst drives NO$_3^-$ reduction and Gly oxidation at the positive electrode, while Zn foil serves as the negative electrode. The cell holds a steady open-circuit voltage of ~1.30 V ($vs.$ Zn^{2+}/Zn) for 24 h, confirming that the paired half-reactions are thermodynamically compatible. Importantly, the introduction of glycerol minimally impacts the electrochemical behaviors of catalysts in the NO$_3$RR, as evidenced by the open circuit potential (OCP) and rate performance of the as-assembled conventional ZNBs (Fig. S12). Discharge curves at increasing current densities (0.5–10 mA cm^{-2}) show well-defined voltage plateaus and excellent rate performance. Upon returning to low-current operation, the discharge voltage recovers to its initial level, indicating good reversibility and stability (Fig. 4b). More surprisingly, under full discharge to 0.005 V ($vs.$ Zn^{2+}/Zn), the aZB with the CuO$_x$/NiCoLDH catalyst delivers energy outputs of 31 and 57.2 mWh at 2 and 5 mA cm^{-2}, respectively, confirming its capacity for practical energy delivery (Fig. S13).

The discharge–charge polarization curve reveals that the maximum power density of the rechargeable aZB reaches 5.2 mW cm^{-2}, closely approaching that of conventional ZNBs, confirming that glycerol introduction imposes a negligible impact on discharge power (Fig. 4c and Fig. S14a). Crucially, a significant reduction in charging voltage is observed for the aZB, demonstrating that glycerol oxidation effectively replaces the high-overpotential OER, thereby enhancing charging efficiency (Fig. 4c and Fig. S14b). Compared with conventional ZNBs, the rechargeable aZB exhibits a consistently smaller
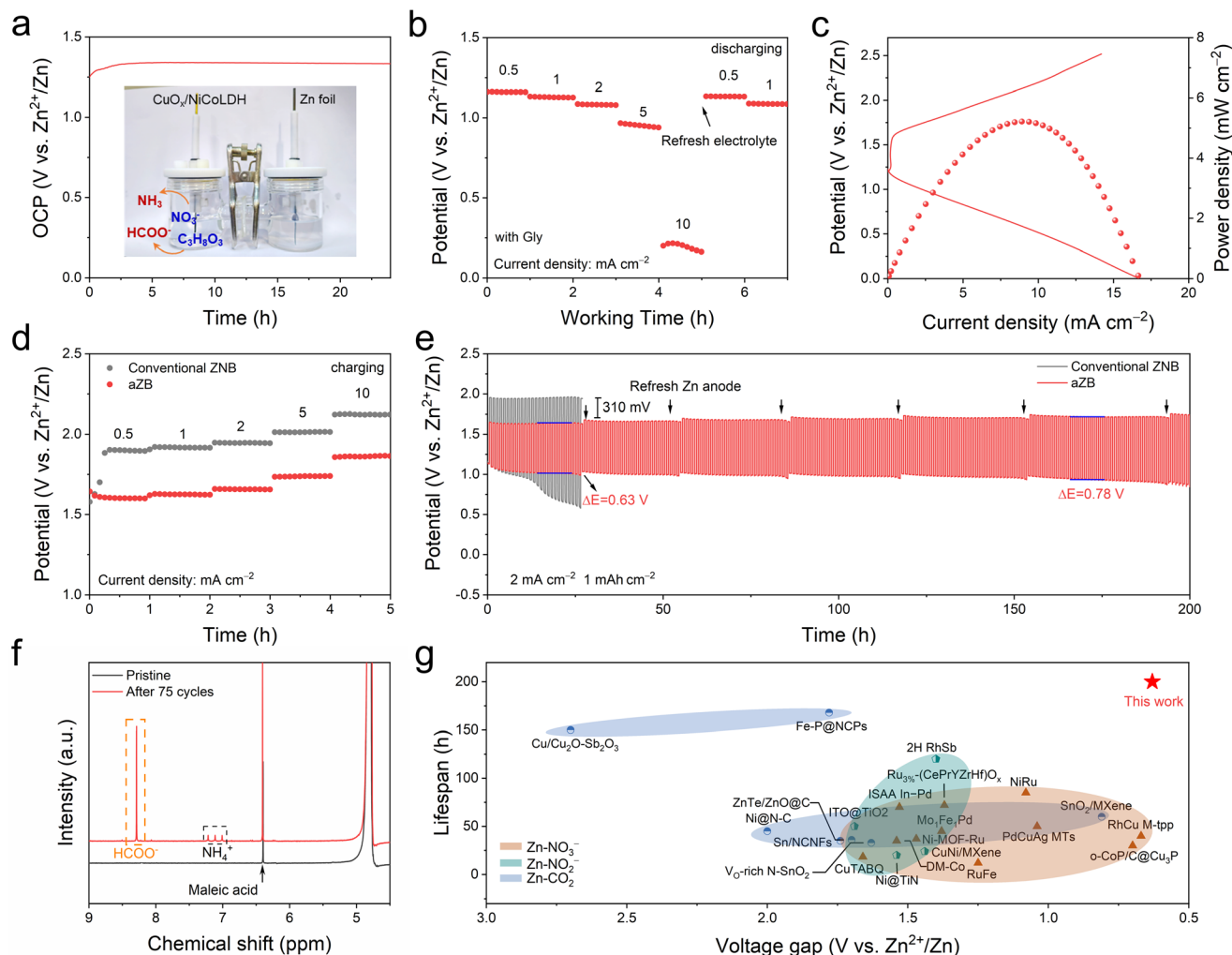
Fig. 4 Electrochemical performance of rechargeable aZBs in an H-type cell. (a) Open circuit potential (OCP) of the aZB based on CuO$_x$/NiCoLDH electrocatalysts. (Inset: photograph of the H-type cell used for simultaneous conversion of nitrate to ammonia and glycerol to formic acid). (b) Rate capability of the aZB with CuO$_x$/NiCoLDH when discharging. (c) Discharge–charge polarization curves and the corresponding power density profiles of the aZB. (d) Galvanostatic charging curves recorded at different current densities (grey: OER-driven; red: GOR-driven). (e) Long-term galvanostatic discharge–charge cycling at 2 mA cm^{-2}. (f) ^{1}H NMR spectra of the catholyte before cycling and after the 75th cycle. (g) Comparison of the performance of the CuO$_x$/NiCoLDH-based aZB with other reported Zn–NO$_3^-$, Zn–NO$_2^-$, and Zn–CO$_2$ batteries.

charge–discharge voltage gap across various current densities, highlighting its improved rechargeability. Distinctly, galvanostatic charging (Fig. 4d) confirms a consistent ~0.30 V drop in charge voltage relative to the OER-driven cell at current densities from 0.5 to 10 mA cm^{-2}, contributing to ~16% energy conservation during the charging process. This indicates that the energy-chemical synergy of aZBs not only produces value-added chemicals but also enhances the overall energy conversion efficiency. Additionally, rate-dependent round-trip charge/discharge tests confirm the remarkable reversibility of the aZB (Fig. S15). The voltage profiles exhibit good recovery after current switching, indicating the robust structural integrity of the CuO$_x$/NiCoLDH catalyst. Notably, the highest round-trip energy efficiency reaches 72.7% at 0.5 mA cm^{-2}, reflecting the highly efficient and stable operation of the aZB under low-rate cycling conditions.

Durability was assessed by continuous charge–discharge cycling at 2 mA cm^{-2} in the H-type cell. The aZBs with the CuO$_x$/NiCoLDH catalyst maintain stable operation for 200 h with no significant voltage decay, aided by periodic Zn foil refreshing (Fig. 4e). Throughout the test, the average voltage gap was 0.63 V, considerably smaller than the 0.94 V of the OER-based ZNB, yielding a round-trip efficiency of 61.8% *versus* 51.7%. Even after 200 h of cycling, the aZB retains 54.4% energy efficiency, highlighting its durability. The voltage profiles of both GOR- (aZB) and OER-driven (ZNB) batteries over long-term cycling are presented in Fig. S16. The results demonstrate that the ZNB exhibits higher charging voltages than the aZB. Furthermore, with increasing cycle number, the ZNB shows a significant decrease in discharge voltage, indicative of pronounced electrochemical polarization. This progressive voltage divergence and increasing polarization further
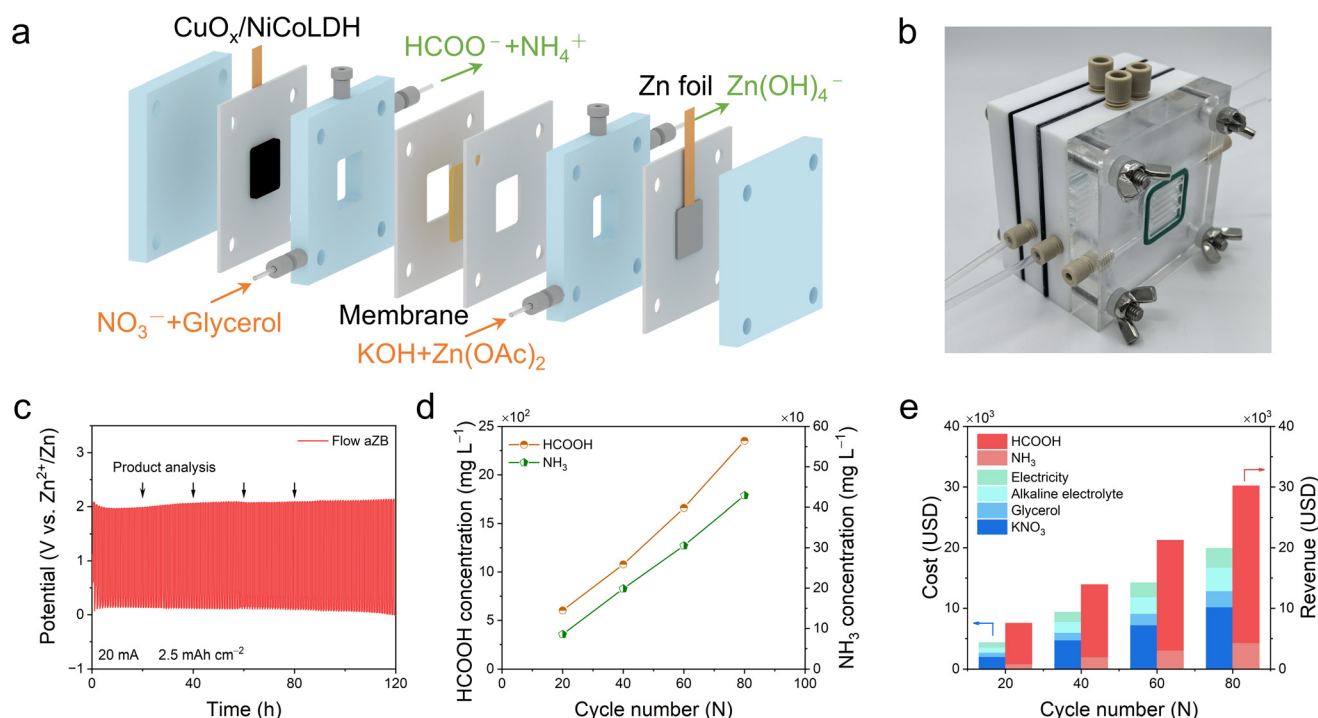
Fig. 5 Electrochemical performance of the rechargeable asymmetric Zn–nitrate/glycerol battery in a flow cell. (a) Schematic illustration of the flow battery setup. (b) Optical photograph of the assembled cell. (c) Long-term galvanostatic discharge–charge cycling curves at 5 mA cm^{-2}. (d) Concentrations of NH$_3$ and formic acid were measured in selected cycles. (e) Techno-economic analysis of NH$_3$ and formic acid co-production in the aZB system.

confirm the superior electrochemical stability of the GOR pathway. Notably, the corresponding discharge/charge products were also investigated. The post-cycling ^{1}H NMR spectra confirm the co-production of NH$_3$ and HCOOH in the cathodic electrolyte (Fig. 4f), validating dual chemical-electricity output. Unlike the most relevant Zn-based batteries, the as-designed rechargeable aZBs achieve the whole-process chemical production during discharge and charge processes. Critically, the aZB outperforms most reported Zn–NO$_3^-$, Zn–NO$_2^-$, and Zn–CO$_2$ systems in terms of voltage gap and operational lifespan, positioning it as a high-efficiency, durable energy–chemical co-production platform (Fig. 4g and Table S1).

To further probe the practical applicability of the concept, we assembled a flow aZB with separate catholyte and anolyte reservoirs and continuous circulation driven by peristaltic pumps (Fig. 5a and b). The disassembled cell with optical photographs of the key components is provided for clarity (Fig. S17). The anolyte was 1 M KOH/0.02 M Zn(CH$_3$COO)$_2$ and the catholyte was 1 M KOH/0.5 M KNO$_3$/0.5 M glycerol. In the early stage, the NH$_4^+$/NH$_3$ and HCOOH/HCOO$^-$ pairs may provide a certain buffering effect to stabilize the local pH, which helps maintain smooth electrochemical reactions. During long-term cycling, this configuration addresses concentration polarization and sustains reactant supply, which is critical for industrial-scale operation. Operated at 5 mA cm^{-2} for 120 h, the flow cell sustained regular charge–discharge cycling (Fig. 5c). Product analysis of the circulating catholyte

by UV-vis and ^{1}H NMR (Fig. 5d) shows steadily rising concentrations of NH$_3$ and HCOOH, demonstrating *in situ* enrichment during extended operation. A techno-economic analysis was performed for the aZB system (Fig. 5e, Table S2 and Note S1). To demonstrate scalability, we presented the scale-up of the system based on its laboratory-scale performance in a flow cell. The assessment considered only the cost of input chemicals and electricity. The results indicate that producing NH$_3$ together with stoichiometric HCOOH would cost less than the combined market value of the two products, yielding an estimated profit of US\$10 257 ($\approx$\$2385 per tonne of NH$_3$) after 80 cycles, which is also compared with electrolyzers (Table S3). These findings suggest that continuous electrosynthesis of NH$_3$ and HCOOH in the aZB flow configuration is both technically viable and economically attractive, demonstrating the commercial potential of the paired-valorization strategy.

Conclusion

In summary, we propose a rechargeable aZB system that couples nitrate reduction and glycerol oxidation through discharge and charge processes to achieve simultaneous energy storage and value-added chemical production. This design replaces the energy-intensive oxygen evolution reaction with a thermodynamically favorable glycerol oxidation reaction, significantly lowering the charging voltage and enhancing energy

efficiency. Assisted by a bifunctional CuO_x/NiCoLDH catalyst, the aZB achieves an energy efficiency of 62.2% and stable operation for over 200 h. This system co-generates NH_3 and HCOOH as valuable chemical outputs during discharge and charge, respectively. TEA confirms the economic viability of our aZB system for industrial, continuous, and profitable electrosynthesis of valuable products. This work establishes a new paradigm for asymmetric battery design that bridges energy conversion and biomass-derived molecule valorization, paving the way for dual-function energy–chemical systems beyond conventional aqueous batteries.

Author contributions

C. Y. and F. W. supervised the project. C. Y. and Z. Y. conceived the idea. Z. Y. and F. W. designed the experiments. Z. Y. and S. C. performed the experiments and analyzed the data. W. M., Y. W. and Y. Q. helped with the catalytic experiments. H. G., F. L. and Z. L. helped with the XRD and TEM characterization. Z. Y., F. W. and C. Y. organized and wrote the manuscript. All authors contributed to the discussion and revision of the manuscript.

Conflicts of interest

The authors declare no conflict of interest.

Data availability

All data needed to evaluate the conclusions in the paper are present in the paper and the accompanying supplementary information (SI) or available from the corresponding authors on reasonable request. The supporting information includes: methods, detailed electrochemical profiles, notes and tables. See DOI: https://doi.org/10.1039/d5eb00163c.

Acknowledgements

References

1 L. Ma, M. A. Schroeder, O. Borodin, T. P. Pollard, M. S. Ding, C. Wang and K. Xu, *Nat. Energy*, 2020, **5**, 743–749.

2 F. Wang, J. Zhang, H. Lu, H. Zhu, Z. Chen, L. Wang, J. Yu, C. You, W. Li, J. Song, Z. Weng, C. Yang and Q.-H. Yang, *Nat. Commun.*, 2023, **14**, 4211.

3 S. Liu, J. Vongsvivut, Y. Wang, R. Zhang, F. Yang, S. Zhang, K. Davey, J. Mao and Z. Guo, *Angew. Chem., Int. Ed.*, 2022, **62**, e202215600.

4 M. Shi, T. Sun, W. Zhang, Q. Nian, Q. Sun, M. Cheng, J. Liang and Z. Tao, *Angew. Chem., Int. Ed.*, 2024, **63**, e202407659.

5 Y. Zuo, Z. Wang, M. Liu, L. Lu, Y. Jiang, J. Lei, H. Yan, H. Li, W. Yan and J. Zhang, *Energy Environ. Sci.*, 2025, **18**, 7490–7503.

6 Z. Chen, F. Wang, R. Ma, W. Jiao, D. Li, A. Du, Z. Yan, T. Yin, X. Yin, Q. Li, X. Zhang, N. Yang, Z. Zhou, Q.-H. Yang and C. Yang, *ACS Energy Lett.*, 2024, **9**, 2858–2866.

7 Y. Guo, R. Zhang, S. Zhang, Y. Zhao, Q. Yang, Z. Huang, B. Dong and C. Zhi, *Energy Environ. Sci.*, 2021, **14**, 3938–3944.

8 W. Yu, J. Yu, M. Huang, Y. Wang, Y. Wang, J. Li, H. Liu and W. Zhou, *Energy Environ. Sci.*, 2023, **16**, 2991–3001.

9 Z. Chang, G. Meng, Y. Chen, C. Chen, S. Han, P. Wu, L. Zhu, H. Tian, F. Kong, M. Wang, X. Cui and J. Shi, *Adv. Mater.*, 2023, **35**, 2304508.

10 H. Jiang, G. F. Chen, O. Savateev, J. Xue, L. X. Ding, Z. Liang, M. Antonietti and H. Wang, *Angew. Chem., Int. Ed.*, 2023, **62**, e202218717.

11 W. Yu, Y. Wang, H. Tan, M. Huang, J. Yu, L. Chen, J. Wang, H. Liu and W. Zhou, *Adv. Energy Mater.*, 2024, **14**, 2402970.

12 H. Guo, Z. Guo, G. Xue, H. Wang, J. Gong, K. Chu, J. Qin, Y. Guan, H. Dong, Y. Chen, Y. E. Miao, C. Zhang, H. Liu, T. Liu, J. Hofkens and F. Lai, *Adv. Mater.*, 2025, **37**, 2500224.

13 L. Sun, H. Yao, Y. Wang, C. Zheng and B. Liu, *Adv. Energy Mater.*, 2023, **13**, 2303054.

14 C. Ma, H. Zhang, J. Xia, X. Zhu, K. Qu, F. Feng, S. Han, C. He, X. Ma, G. Lin, W. Cao, X. Meng, L. Zhu, Y. Yu, A.-L. Wang and Q. Lu, *J. Am. Chem. Soc.*, 2024, **146**, 20069–20079.

15 J. Li, L. Liu, S. Huang, H. Wang, Y. Tang, C. Zhang, F. Du, R. Ma, C. Li and C. Guo, *Adv. Funct. Mater.*, 2025, **35**, 2501527.

16 S. Chen, K. Lian, W. Liu, Q. Liu, G. Qi, J. Luo and X. Liu, *Nano Res.*, 2023, **16**, 9214–9230.

17 J. Zhou, Y. Xiong, M. Sun, Z. Xu, Y. Wang, P. Lu, F. Liu, F. Hao, T. Feng, Y. Ma, J. Yin, C. Ye, S. Xi, Y. Zhu, B. Huang and Z. Fan, *Proc. Natl. Acad. Sci. U.S.A.*, 2023, **120**, e2311149120.

18 Y. Liu, Y. An, J. Zhu, L. Zhu, X. Li, P. Gao, G. He and Q. Pang, *Nat. Commun.*, 2024, **15**, 977.

19 H. Jiang, G. F. Chen, G. Hai, W. Wang, Z. Liang, L. X. Ding, Y. Yuan, J. Lu, M. Antonietti and H. Wang, *Angew. Chem., Int. Ed.*, 2023, **62**, e202305695.

20 G. Yang, Y. Jiao, H. Yan, Y. Xie, A. Wu, X. Dong, D. Guo, C. Tian and H. Fu, *Adv. Mater.*, 2020, **32**, 2000455.

21 M. Zhang, P. Zou, G. Jeerh, B. Sun, M. Walker and S. Tao, *Adv. Funct. Mater.*, 2022, **32**, 2204881.

22 F. Ye, S. Zhang, Q. Cheng, Y. Long, D. Liu, R. Paul, Y. Fang, Y. Su, L. Qu, L. Dai and C. Hu, *Nat. Commun.*, 2023, **14**, 2040.

23 T. Wang, X. Cao and L. Jiao, *Angew. Chem., Int. Ed.*, 2022, **61**, e202213328.

24 X. Pan, L. Sun, Z. Zhou, Y. Xie, J. Zheng, S. Xu, J. Sun, J. Zeng and G. Zhao, *Adv. Energy Mater.*, 2024, **14**, 2400374.

25 C. Li, H. Li, B. Zhang, H. Li, Y. Wang, X. Wang, P. Das, Y. Li, X. Wu, Y. Li, Y. Cui, J. Xiao and Z. S. Wu, *Angew. Chem., Int. Ed.*, 2024, **63**, e202411542.

26 L. Fan, Y. Ji, G. Wang, J. Chen, K. Chen, X. Liu and Z. Wen, *J. Am. Chem. Soc.*, 2022, **144**, 7224–7235.

27 R.-Y. Fan, X.-J. Zhai, W.-Z. Qiao, Y.-S. Zhang, N. Yu, N. Xu, Q.-X. Lv, Y.-M. Chai and B. Dong, *Nano-Micro Lett.*, 2023, **15**, 190.

28 S. Wang, Y. Lin, Y. Li, Z. Tian, Y. Wang, Z. Lu, B. Ni, K. Jiang, H. Yu, S. Wang, H. Yin and L. Chen, *Nat. Nanotechnol.*, 2025, **20**, 646–655.

29 Q. Zhang, X. Zhang, B. Liu, P. Jing, X. Xu, H. Hao, R. Gao and J. Zhang, *Angew. Chem., Int. Ed.*, 2025, **64**, e202420942.

30 V. Andrei, I. Roh, J.-A. Lin, J. Lee, Y. Shan, C.-K. Lin, S. Shelton, E. Reisner and P. Yang, *Nat. Catal.*, 2025, **8**, 137–146.

31 S. Li, P. Ma, C. Gao, L. Liu, X. Wang, M. Shakouri, R. Chernikov, K. Wang, D. Liu, R. Ma and J. Wang, *Energy Environ. Sci.*, 2022, **15**, 3004–3014.

32 J. Wang, H. T. D. Bui, H. Hu, S. Kong, X. Wang, H. Zhu, J. Ma, J. Xu, Y. Liu, L. Liu, W. Chen, H. Bi, M. Yang, F. Huang, T. Brinck and J. Wang, *Adv. Mater.*, 2025, **37**, 2418451.

33 Q. Qian, Y. Zhu, N. Ahmad, Y. Feng, H. Zhang, M. Cheng, H. Liu, C. Xiao, G. Zhang and Y. Xie, *Adv. Mater.*, 2023, **36**, 2306108.

34 W. Gao, C. Wang, W. Wen, S. Wang, X. Zhang, D. Yan and S. Wang, *Adv. Mater.*, 2025, **37**, 2503198.

35 J. Cheng, L. Wu and J. Luo, *Nat. Commun.*, 2023, **14**, 7228.

36 M. Li, Q. Shi, Z. Li, M. Xu, S. Yu, Y. Wang, S. M. Xu and H. Duan, *Angew. Chem., Int. Ed.*, 2024, **63**, e202406515.

37 K. A. Owusu, Z. Wang, A. Saad, F. O. Boakye, M. A. Mushtaq, M. Tahir, G. Yasin, D. Liu, Z. Peng and X. Cai, *Energy Environ. Mater.*, 2023, **7**, e12545.

38 Q. Hu, K. Yang, O. Peng, M. Li, L. Ma, S. Huang, Y. Du, Z.-X. Xu, Q. Wang, Z. Chen, M. Yang and K. P. Loh, *J. Am. Chem. Soc.*, 2023, **146**, 668–676.

39 Z. Ren, K. Shi and X. Feng, *ACS Energy Lett.*, 2023, **8**, 3658–3665.

40 N. Zhou, Z. Wang, N. Zhang, D. Bao, H. Zhong and X. Zhang, *ACS Catal.*, 2023, **13**, 7529–7537.

41 J.-Y. Fang, Q.-Z. Zheng, Y.-Y. Lou, K.-M. Zhao, S.-N. Hu, G. Li, O. Akdim, X.-Y. Huang and S.-G. Sun, *Nat. Commun.*, 2022, **13**, 7899.

42 W. Jang, D. Oh, J. Lee, J. Kim, J. E. Matthews, H. Kim, S.-W. Lee, S. Lee, Y. Xu, J. M. Yu, S. W. Hwang, T. F. Jaramillo, J.-W. Jang and S. Cho, *J. Am. Chem. Soc.*, 2024, **146**, 27417–27428.

43 K.-H. Kim, H. Lee, X. Huang, J. H. Choi, C. Chen, J. K. Kang and D. O'Hare, *Energy Environ. Sci.*, 2023, **16**, 663–672.

44 Y. Qie, J. Gao, S. Li, M. Cui, X. Mao, X. Wang, B. Zhang, S. Chi, Y. Jia, Q.-H. Yang, C. Yang and Z. Weng, *Sci. China Mater.*, 2024, **67**, 2941–2948.